Structural Studies of Tin-Doped Indium Oxide (ITO) and In$_4$Sn$_3$O$_{12}$

N. Nadaud,[1] N. Lequeux, and M. Nanot

*Laboratoire Céramiques et Matériaux Minéraux, UA–CNRS Matériaux Inorganiques, Ecole Supérieure de Physique et de Chimie Industrielles de Paris,
10 Rue Vauquelin, F-75231 Paris Cedex 05, France*

J. Jové

Institut Curie, Section de Recherche, 26 Rue d'Ulm, F-75231 Paris Cedex 05, France

and

T. Roisnel

Laboratoire Léon Brillouin (CEA/CNRS), Centre d'Etudes de Saclay, F-99191 Gif-sur-Yvette, France

Structural changes in the indium oxide lattice due to doping with Sn^{4+} (ITO) were studied by Mössbauer spectroscopy, EXAFS, and neutron powder diffraction. There is a decrease in electrical conductivity as the tin content and oxygen partial pressure increase, which is related to a distortion in the first Sn–O shell. Doping with tin increases the oxygen/cation ratio and the lattice parameter and decreases the Sn–O distances, which disorders the host network. The low-conduction In$_4$Sn$_3$O$_{12}$ phase precipitates when the tin content exceeds 6 at.%. In$_4$Sn$_3$O$_{12}$ is rhombohedral (space group $R\bar{3}$, $a = 9.4604(2)$ Å, and $c = 8.8584(2)$ Å in a hexagonal basis). There is a cation ordering with octahedral sites fully occupied by tin, the tin sites being equivalent in both highly doped ITO and In$_4$Sn$_3$O$_{12}$. © 1998 Academic Press

1. INTRODUCTION

Thin films of tin-doped indium oxide (ITO, for indium–tin oxide) exhibit high electrical conductivity (up to $10^4 \ \Omega^{-1} \cdot \text{cm}^{-1}$), high transparency in the visible range, and high infrared reflectivity for wavelengths higher than 1 μm. ITO films are used as transparent electrodes in liquid-crystal displays and heat reflection filters (1). ITO is a wide-gap, degenerate semiconductor where electrons are the major charge carriers. The Sn atoms are considered to substitute for In, without ordering. The difference of valence between In^{3+} and Sn^{4+} results in the donation of a free electron to the lattice. For most applications, ITO films must be as

conducting as possible, which requires a high carrier density (N) and a high carrier mobility (μ). The electrical and optical properties of ITO films (tin content less than 10 at.%) have been extensively studied (2–4). The main features are as follows:

(i) Oxidizing conditions decrease the carrier concentration, whatever the tin content. The introduction of tin into In$_2$O$_3$ is considered to facilitate the migration of interstitial oxygens within the anionic sublattice. For low-doped ITO films prepared by a spray technique, Frank and Köstlin (4) suggested the presence of neutral clusters ("Sn$_2 \cdot$O$_i$"), which trap the free carriers. These clusters can be eliminated by thermal treatments in a reducing atmosphere.

(ii) The carrier concentration is at a maximum for 6–8 at.% Sn (4–6) and decreases beyond this limit. The neutralization of the tin donor effect is found whatever the oxygen partial pressure but is enhanced by highly oxidizing conditions. Frank and Köstlin (4) suggested that an increase in the tin content or the oxygen partial pressure leads to the formation of nonreducible fluorite-type Sn$_2$O$_4$ clusters. In contrast, Parent *et al.* (5) showed by X-ray absorption spectroscopy on ITO films prepared by a pyrolysis technique that the presence of tin disorganizes the host network and relaxes the oxygen environment toward a configuration which is similar to that of rhomboedral In$_2$O$_3$ (for indium cations) and SnO$_2$ (for tin cations). Shigesato *et al.* (7) showed that tin can segregate close to the film surface or along grain boundaries to form an insulating phase.

There are numerous studies on ITO films, but few on ITO sintered ceramics. The solubility limit of tin in In$_2$O$_3$ ceramics is not known with precision but has been estimated to be between 6 and 11% Sn (6, 8–11) For the rest of the paper,

[1] To whom correspondence should be addressed.

the dopant content will always be expressed as atomic percent, i.e., [dopant]/([dopant] + [In]). The existence of a tin-rich compound of fixed composition ($In_4Sn_3O_{12}$, i.e., $2In_2O_3$–$3SnO_2$) has been reported (10–12), but we lack structural information on this compound and on the tin neutralization effect.

In the present study, the local environment of tin in ITO ceramics (tin content from 0 to 9%) has been investigated by Mössbauer spectroscopy and EXAFS. The crystal structure of $In_4Sn_3O_{12}$ has been clarified. We have tried to establish the relationship between the tin atomic environment and the electrical properties of the considered materials, i.e., $In_4Sn_3O_{12}$ and ITO, using Mössbauer, EXAFS, and neutron diffraction data. Finally, the models proposed for ITO films (4, 5, 7) are discussed.

EXPERIMENTAL

Preparation of Ceramics

ITO materials with 0.5–9% Sn were prepared from powdered mixtures of 99.99 wt% pure In_2O_3 (Metaleurop Recherche) and 99.9 wt% pure SnO_2 (Merck) calcined at 1400°C for 3 h in either a reducing atmosphere ($pO_2 = 2 \times 10^{-3}$ atm) or an oxidizing atmosphere ($pO_2 = 1$ atm) (13).

$In_4Sn_3O_{12}$ was prepared by reacting In_2O_3 and SnO_2 powders at 1550°C for 10 h and then quenching in air. To prevent volatilization of the materials, the green bodies were compacted and then placed in a bed of prereacted $In_4Sn_3O_{12}$ powders. The solubility limit of tin in In_2O_3 and the phase purity of $In_4Sn_3O_{12}$ were determined by X-ray powder diffraction.

Mössbauer Spectroscopy

The Mössbauer source was 10 mCi of Ca $^{119}SnO_3$ (Amersham). To filter the Sn$K\alpha$ X-rays, a 0.05-mm Pd foil was placed in front of the samples. The spectra were recorded using a constant acceleration type spectrometer. Calibration velocity was accomplished using a 25-mCi ^{57}Co source. SnO_2 spectra were recorded to reference the isomer shift. Absorption experiments were carried out with a conventional device.

Neutron and X-Ray Powder Diffraction

X-ray diffraction data were recorded at room temperature on a Philips PW1710 diffractometer (Cu$K\alpha$). Neutron diffraction experiments were performed at room temperature at the Orphée reactor (Saclay, France) with the 3T2 high-resolution powder diffractometer ($\lambda = 1.2272$ Å). Data were analyzed by the Fullprof Rietveld-type program (14), taking into account indium neutron absorption by a previously measured transmission coefficient.

X-Ray Absorption Spectroscopy

EXAFS experiments were conducted at LURE (Orsay, France) using the synchrotron radiation from the DCI storage ring. EXAFS spectra of In_2O_3, SnO_2, ITO (6% Sn), and $In_4Sn_3O_{12}$ were recorded at room temperature in the transmission mode at the In (27,940 eV) and Sn (29,200 eV) K-edges using a Ge(400) double-crystal monochromator. Incident and transmitted beam intensities were measured using krypton-filled ionization chambers. When possible, the sample thickness was chosen such that $\Delta\mu x = 1$, an edge jump of $\Delta\mu x = \frac{1}{10}$ being used for ITO samples studied at the Sn edge to limit the absorption by indium. The EXAFS oscillations were extracted from the whole spectrum by subtracting a spline-fitted background (which describes the atomic absorption) and normalizing to the height of the edges. The edge energies were chosen at half-height of the absorption jump. The $\chi(E)$ line was normalized to the pre-edge absorption by fitting a first-order polynomial extrapolated to the EXAFS area. The $k^3\chi(k)$ signal was Fourier transformed over the 3.5- to 14-Å^{-1} (10.5 Å^{-1} for ITO at the Sn K-edge) k range, using a Kaiser–Bessel window ($\tau = 3$). The phase shifts and backscattering amplitudes of In and Sn were extracted from In_2O_3 and SnO_2 spectra and fitted to the back-transformed data corresponding to a particular shell (In–O or Sn–O) using the program FITEX (15).

RESULTS AND DISCUSSION

In_2O_3–SnO_2 Phase Diagram

The lattice parameters for a body cubic centered ITO solid solution were plotted versus the tin content (Fig. 1). The lattice parameters were deduced from Rietveld refinement of X-ray and neutron powder diffraction profiles. As
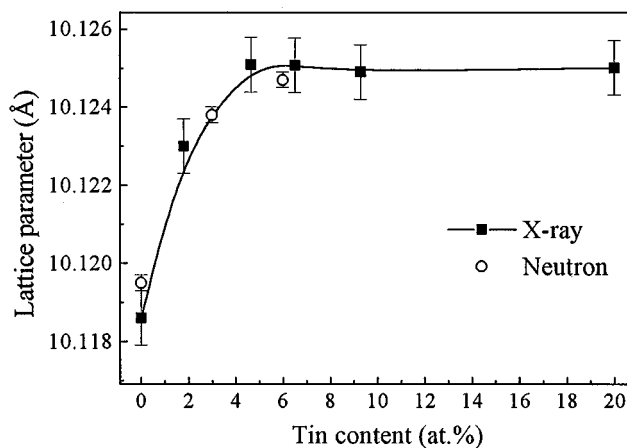

FIG. 1. Lattice parameters of Sn-doped In_2O_3 materials as given by X-ray and neutron powder diffraction data (ceramics sintered at 1400°C for 3 h in an oxygen atmosphere).

previously reported (8, 11), the tin doping (up to 5–6% Sn) leads to an increase in the lattice constant. This is in contradiction with Vegard's law, which predicts a linear decrease in the lattice parameter as the tin content increases [the Sn^{4+} ionic radius (0.71 Å) is smaller than that of In^{3+} (0.81 Å)]. There is no change in lattice parameter for tin content greater than 6 at.% and the presence of an $In_4Sn_3O_{12}$ phase is detected by X-ray powder diffraction data (10–12). This indicates that the solubility limit of tin in indium oxide at 1400°C must be close to 6 %, as previously found for films (4) and ceramics (11).

Electrical Properties of ITO Ceramics

Figure 2 shows a plot of carrier density versus tin content in ITO ceramics (6), single crystals (16), and thin films (3, 5, 17). The carrier density no longer follows the expected behavior (one electron for each tin added, as represented by a dotted straight line). In fact, the carrier concentration shows a plateau (for tin contents depending on elaboration method) and, finally, decreases for higher tin contents. A strong correlation is found between the solubility limit of tin in those materials and the tin content corresponding to the carrier density maximum, which suggests that the electrical properties closely depend on structural changes. However, the presence of low-conduction $In_4Sn_3O_{12}$ precipitates must also be involved in the decrease in carrier concentration in ITO ceramics with tin contents greater than 6%. Nevertheless, the reason for the low efficiency of tin as a carrier donor in single-phase ITO remains unclear.
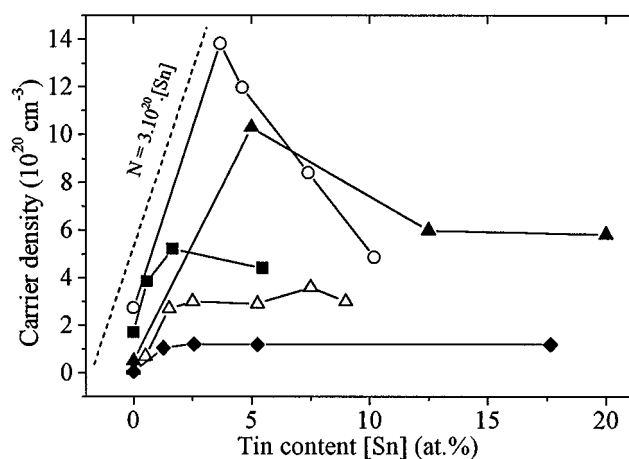
Tin Environment in ITO

In_2O_3 exhibits the cubic bixbyite structure (C-type, rare-earth sesquioxide structure: $Ia\bar{3}$ space group, No. 206). It shows a fluorite-related superstructure (18) where one-fourth of the anions are missing. Indium cations are located in two different six-fold-coordinated sites (Fig. 3). One-fourth of the cations are located in trigonally compressed octahedra (b site, symmetry $\bar{3}$, In–O distance: 2.18 Å). The remaining three-fourths are located in highly distorted octahedra (d site, symmetry 2, set of three In–O distances: 2.13, 2.19, and 2.23 Å). Each cationic site can be described as a cube where two anion sites are empty at opposite vertices for b sites and along one diagonal of a face for d sites. The structural oxygen vacancies are located along the four $\langle 111 \rangle$ axes.

^{119}Sn Mössbauer spectroscopy, X-ray absorption, and neutron diffraction were used to study the environment of tin in ITO ceramics. The aim was to correlate structural features with dopant concentration and oxygen partial pressure.

The ^{119}Sn Mössbauer spectra of Sn-doped In_2O_3 (0.5–9% Sn, sintered in either O_2 or N_2 atmospheres) and $In_4Sn_3O_{12}$ are presented in Figs. 4a and 4b. The best fits (i.e., with the lowest χ^2) are obtained by assuming the presence of two doublets. The fits with one doublet are unacceptable and those with two doublets and a singlet do not improve the fit significantly. The Mössbauer parameters are given in Table 1. Isomer shift (δ) is sensitive to the effective number of 5s and 5p electrons present in the bonding. Isomer shifts for compounds of tetravalent tin range from about -0.6 mm·s^{-1} for the essentially covalent compounds, to about $+1.5$ mm·s^{-1} for fully ionic compounds. It is obvious that only Sn^{IV} is detected in ITO compounds, as δ lies from 0.1 to 0.4 mm·s^{-1}.

FIG. 2. Carrier density (N) versus tin content in ITO thin films [(○) (3), (▲) (5), (■) (17)], single crystals [(△) (16)], and ceramics [(◆) (6)]. The dotted line ($N = 3 \times 10^{20}$ [Sn]) represents the carrier density if each tin provides one free electron.

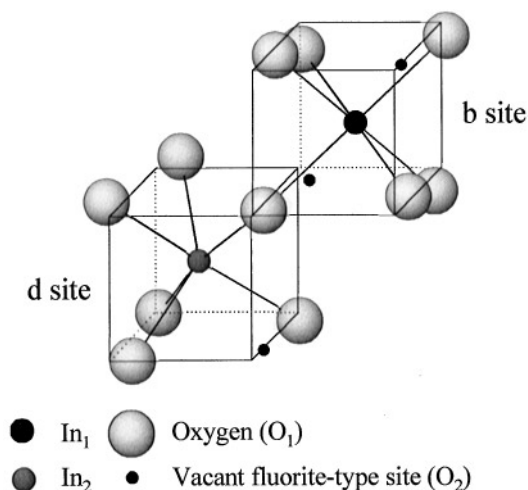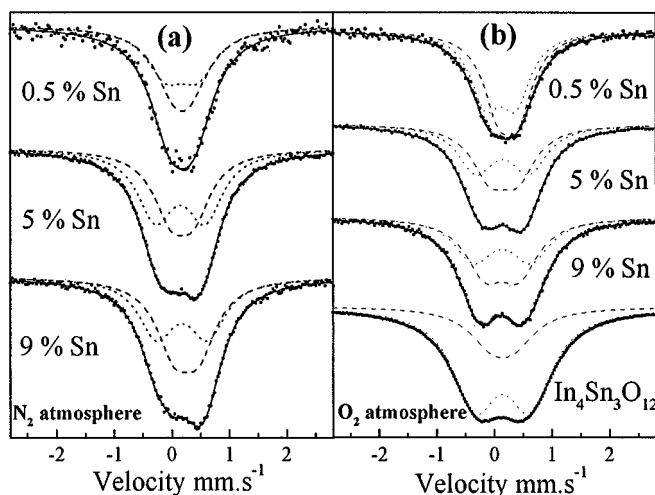**FIG. 3.** Cationic sites in the cubic In_2O_3 structure.

FIG. 4. ^{119}Sn Mössbauer spectra for ITO (0.5, 5, and 9% Sn) and $In_4Sn_3O_{12}$ treated in an O_2 (a) or N_2 (b) atmosphere.
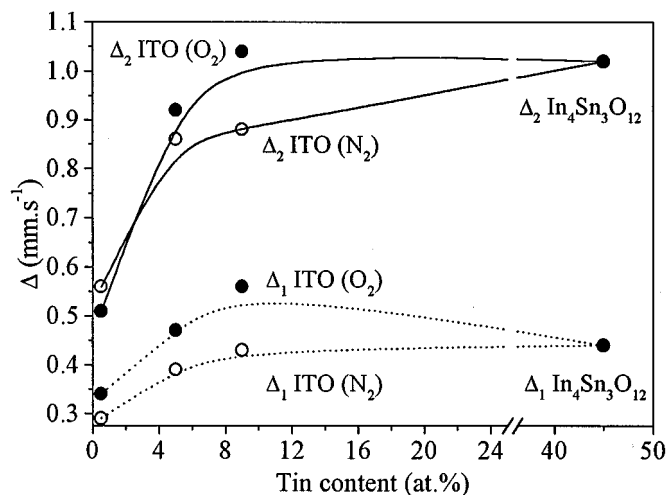

FIG. 5. Quadrupole splitting (Δ) versus dopant content for In_2O_3–SnO_2 materials sintered at 1400°C for 3 h in an O_2 or N_2 atmosphere.

The quadrupole splitting (Δ) arises from two main components: one due to the valence electrons of the transition-metal ion, which are not spherically symmetric, and another due to the electrostatic contribution of the neighbor oxygen ions (pure ionic lattice account). The values of Δ in ITO are sensitive to the tin content and oxygen partial pressure as shown in Fig. 5. The value of Δ that corresponds to site 1 (Δ_1) or site 2 (Δ_2) increases as the tin content increases, whatever the pO_2. Highly oxidizing conditions lead to higher Δ values than reducing ones. Finally, the quadrupolar splitting relative to $In_4Sn_3O_{12}$ is similar to what is found in highly doped ITO.

We attribute Δ_1 and Δ_2 to sites b and d, respectively (19), in agreement with the results of Nomura *et al.* (20) but in contradiction with the results of refs 21 and 22. More information is needed to correlate the Δ data and the

indium oxide crystallographic data without ambiguity. However, using the area ratio given by the Mössbauer data (see Table 1), we consider that the tin occupies the less distorted b site rather than the d site. Independently of the site attribution, the Δ changes suggest major changes in the environment of tin as the dopant content and pO_2 increase. The insertion of tin leads to a progressive distortion of the first tin–oxygen shell toward a configuration close to that of $In_4Sn_3O_{12}$.

EXAFS was used to clarify the difference between the tin environment and the indium environment. The k^3-weighted Fourier transform and the structural parameters for the first oxygen shell around the cations in In_2O_3, SnO_2, and ITO (6% Sn, sintered in oxygen) are given in Fig. 6 and Table 2,

TABLE 1
Mössbauer Parameters in In_2O_3–SnO_2 Materials

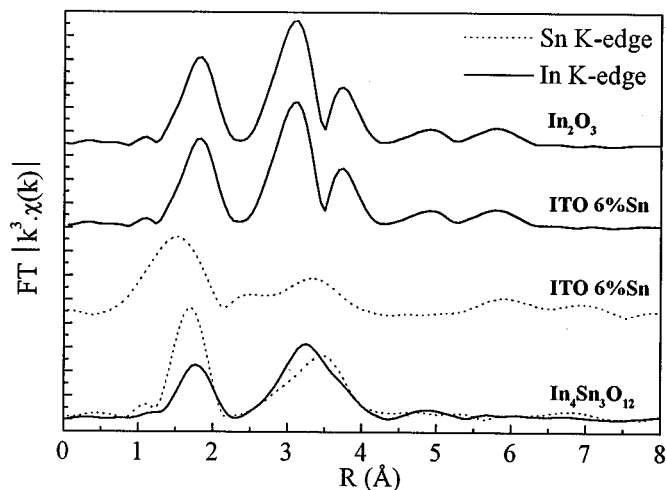| Doping content	pO_2 (atm)	$\delta \pm 0.02$ (mm·s^{-1})	$\Delta \pm 0.02$ (mm·s^{-1})	Area $\pm$ 0.3 (%)	$\Gamma \pm 0.01$ (mm·s^{-1})	χ^2
0.5% Sn	1	0.25	0.34	50.9	0.78	0.99
		0.11	0.51	49.1		
	2×10^{-3}	0.18	0.29	53.0	0.81	0.92
		0.17	0.56	47.0		
5% Sn	1	0.17	0.47	50.4	1.15	0.72
		0.14	0.92	49.6		
	2×10^{-3}	0.18	0.39	45.8	0.75	0.93
		0.15	0.86	54.2		
9% Sn	1	0.18	0.56	55.0	1.25	0.80
		0.18	1.04	45.0		
	2×10^{-3}	0.25	0.43	53.0	0.75	1.08
		0.18	0.88	47.0		
45% Sn	—	0.16	0.44	25.0	2.20	0.66
$In_4Sn_3O_{12}$		0.14	1.02	75.0		

FIG. 6. k^3-weighted Fourier transforms for In_2O_3, SnO_2, ITO (6% Sn, Sn K-edge), and $In_4Sn_3O_{12}$ (both In and Sn K-edges).

TABLE 2
Parameters of the First (In/Sn)–O Contribution as Determined by EXAFS

	EXAFS data					Structural data		
	R_1 (Å)[a]	N_1[b]	$2(\Delta\sigma)^2$ (10^{-3} Å^2)	ΔE_0 (eV)	χ^2		R_{cryst} (Å)	N_{cryst}
ITO 6% Sn, In edge	2.18	5.9	2.6	−0.07	0.72	In_2O_3	2.18	6
ITO 6% Sn, Sn edge	2.00	6.1	5.4	0.41	3.90			
$In_4Sn_3O_{12}$, In edge	2.16	5.1	4.4			$In_4Sn_3O_{12}$		
	2.52	1.3	9.2	1.92	0.99	$M1$	2.06	6
						$M2$	2.07–2.64	7
$In_4Sn_3O_{12}$, Sn edge	2.05	5.8	4.1	1.32	1.11			

[a] Shell radius.
[b] Coordination number.

respectively. The coordination does not seem modified with the presence of Sn ($R = 2.18$ Å, $N = 5.9$ in 6% Sn: In_2O_3). We did not find a splitting of the In–O distance into two contributions, contrary to what was found by Parent *et al.* (5) in highly doped ITO films (39% Sn). An increase in the relative Debye–Waller factor (In K-edge: $2(\Delta\sigma)^2 = 0.0026$ Å^2) suggests a more highly distorted oxygen environment around indium, due to the insertion of tin.

The Sn–O shell radius is much smaller than the In–O radius in In_2O_3 (2.00 instead of 2.18 Å). This value demonstrates that the tin induces strong modifications in its first oxygen shell, as suggested by Mössbauer spectroscopy. The shortening of the Sn–O distance previously reported in ITO layers () is confirmed in ITO bulk materials. However, an EXAFS analysis is not sufficiently accurate to detect slight changes in the tin coordination. Rietveld refinement of neutron diffraction patterns was conducted on ITO with 0 and 3% Sn (sintered in oxygen) and 6% Sn (sintered in either oxygen or nitrogen). In_2O_3 crystallographic features (18) were used to fit the ITO diffraction data. The occupancy of structural oxygen vacancy [Wyckoff position: $\frac{1}{8}, \frac{1}{8}, \frac{1}{8}$ (V_{fluorite})] was also refined. The atomic positions, B values, refinement parameters, and oxygen occupancies of V_{fluorite} sites are given in Table 3. The structural data are quite similar to those of indium oxide, except for the lattice parameters (see Fig. 1). The differences between the indium (0.41×10^{-12} cm) and tin (0.62×10^{-12} cm) scattering length values are too small and the tin content is too low to allow us to discriminate indium sites from tin sites. Nevertheless, the overall occupancy of the V_{fluorite} site is found to increase as the tin content increases in oxidized ITO materials. In contrast, the V_{fluorite} site occupancy does not significantly change in In_2O_3 or in reduced ITO.

Structure of $In_4Sn_3O_{12}$

Neutron powder diffraction data were indexed in a rhombohedral unit cell with $a = 6.2071(4)$ Å and $\alpha = 99.29°$,

which correspond to $a = 9.4604(2)$ Å and $c = 8.8584(2)$ Å in a hexagonal basis (Fig. 7). The space group was taken as $R\overline{3}$ (No. 148), as reported earlier (11, 12). The parameters deduced from the refinement treatment (considering 514 reflections) were $R_B = 4.4\%$, $R_{wp} = 11.1\%$, and $R_{exp} = 8.4\%$. The Wyckoff positions and the main interatomic distances and angles of the structure are given in Tables 3 and 4, respectively. $In_4Sn_3O_{12}$ is isostructural with a wide range of M_7O_{12} compounds that exhibit a fluorite-related superstructure, in particular Tb_7O_{12} (23), $Yb_4Zr_3O_{12}$ (24), $Sc_4Zr_3O_{12}$ (25), UY_6O_{12} and ULu_6O_{12} (26), Pr_7O_{12} (27, 28), $Sc_4Ti_3O_{12}$, $Er_4Zr_3O_{12}$, and $Sc_4Hf_3O_{12}$ (29). Two nonequivalent cationic sites, labeled $M1$ and $M2$, are found. One-seventh of the cations are located in the $(3a)$ $M1$ site. The coordination of cations in the $M1$ site is six, instead of eight in the ideal fluorite structure. The configuration can be described as either a trigonally compressed octahedron or a distorted cube with empty anionic positions at opposite vertices. The values of angles O–$M1$–O obtained from data refinement (82.9° and 97.1°; see Table 4) are closer to the regular octahedron angles (90°) than to the regular cubic angles (70.5° and 109.5°). In the isostructural compounds, a weakly distorted octahedron is observed around uranium ($r_U^{6+} = 0.80$ Å) in UY_6O_{12} (26) and around titanium ($r_{Ti}^{4+} = 0.68$ Å) in $Sc_4Ti_3O_{12}$ (29), whereas $Yb_4Zr_3O_{12}$ and $Sc_4Zr_3O_{12}$ ($r_{Yb}^{4+} = 0.86$ Å, $r_{Zr}^{4+} = 0.79$ Å) exhibit cubic configurations (24, 25). The relationship between the special-site distortion and the cation radius is not clear.

The $M1$ cation and the two structural oxygen vacancies are located on the inversion-triad axis that coincides with one of the $\langle 111 \rangle_{\text{fluorite}}$ axes (Fig. 8). The building block is an oxygen vacancy pair along the $\overline{3}$ axis, with the center occupied by an $M1$ cation. The polyhedra $M1O_6V_2$ (where V is the formal oxygen vacancy) are isolated from each other. They are located at the three lattice points in the hexagonal basis that are shown in Fig. 8.

The remaining six-sevenths of the $M2$ cations are in $(18f)$ general positions. They are surrounded by seven oxygen

TABLE 3
Structural Data and Refinement Parameters for In_2O_3–SnO_2 Materials as Given by Rietveld Refinement of Neutron Powder Diffraction Patterns

	In_2O_3	ITO 3% Sn (O_2)	ITO 6% Sn (O_2)	ITO 6% Sn (N_2)	$In_4Sn_3O_{12}$
Lattice parameter (Å)	10.1192(2)	10.1234(2)	10.1247(2)	10.1309(2)	$a = 9.4604(2)$ $c = 8.8584(2)$
Cation 1					
x	$\frac{1}{4}$	$\frac{1}{4}$	$\frac{1}{4}$	$\frac{1}{4}$	0
y	$\frac{1}{4}$	$\frac{1}{4}$	$\frac{1}{4}$	$\frac{1}{4}$	0
z	$\frac{1}{4}$	$\frac{1}{4}$	$\frac{1}{4}$	$\frac{1}{4}$	0
B (Å^2)	0.40(7)	0.38(13)	0.46(13)	0.42(11)	0.54(6)
Sn/(In + Sn) (%)	0	3[a]	10(1)	21(1)	100(1)
Cation 2					
x	0.4667(2)	0.4673(2)	0.4678(2)	0.4667(2)	0.2526(2)
y	0.0000	0.0000	0.0000	0.0000	0.2145(2)
z	0.0000	0.0000	0.0000	0.0000	0.3497(2)
B (Å^2)	0.34(4)	0.31(5)	0.38(6)	0.35(5)	0.47(4)
Sn/(In + Sn) (%)	0	3[a]	5(1)	1(1)	32(1)
O_1					
x	0.3909(2)	0.3899(2)	0.3893(2)	0.3901(2)	0.1979(2)
y	0.1543(2)	0.1547(2)	0.1545(2)	0.1545(2)	0.1768(2)
z	0.3820(2)	0.3821(2)	0.3820(2)	0.3820(2)	0.1162(2)
B (Å)	0.45(2)	0.50(2)	0.59(2)	0.51(2)	0.96(4)
O_2					
x	$\frac{1}{8}$	$\frac{1}{8}$	$\frac{1}{8}$	$\frac{1}{8}$	0.1886(3)
y	$\frac{1}{8}$	$\frac{1}{8}$	$\frac{1}{8}$	$\frac{1}{8}$	0.9745(2)
z	$\frac{1}{8}$	$\frac{1}{8}$	$\frac{1}{8}$	$\frac{1}{8}$	0.3917(2)
B (Å^2)	0.45[a]	0.50[a]	0.59[a]	0.51[a]	0.82(3)
Occ (%)[b]	0.2(1)	0.8(1)	3.2(1)	0.1(1)	—
R_{wp} (%)	18.4	14.3	16.2	14.5	11.1
R_{exp} (%)	15.85	12.2	12.4	12.0	8.4
R_B (%)	4.46	3.7	5.8	5.8	4.4

[a] Fixed equal to $B(O_1)$ for fitting.

[b] Occ = oxygen occupancy (%) of "structural" vacancy in the In_2O_3 fluorite-related structure.

atoms, set at the vertices of a highly distorted cube where one corner is lacking ($M2O_7V_1$). The metal–oxygen distances vary widely (from 2.07 to 2.64 Å, average 2.23 Å), the distance $M2$–O being longer than $M1$–O (2.06 Å).

The polyhedra $M1O_6V_2$ and $M2O_7V_1$ can be connected with the so-called "Bevan" cluster (24) where the sixfold-coordinated $M1$ polyhedron is surrounded by six sevenfold-coordinated polyhedra $M2$ with sharing edges. $M1$ and $M2$ polyhedra are stacked along the threefold rotation axis, as shown in Fig. 9.

Neutron diffraction and EXAFS were used to determine whether cation ordering occurs in $In_4Sn_3O_{12}$. Refinement of neutron data suggests that $M1$ sites are fully occupied by tin atoms whereas $M2$ sites are occupied by indium and the remaining tin atoms. EXAFS data of $In_4Sn_3O_{12}$ at the In and Sn K-edges are shown in Figs. 6 and 10. The In and Sn edge EXAFS contributions for the first metal–oxygen shell are rather different. Table 2 shows the EXAFS data-fitting results of the first M–O shell analyzed.

(i) At the In edge, two contributions are needed to refine properly the $k^3\chi(k)$ relative to the first oxygen shell. The first In–O shell is estimated at 2.16 Å (5.1 oxygen atoms) and a second In–O shell at 2.52 Å (1.3 oxygen atoms). This configuration is similar to that of the $M2$ site deduced from neutron powder diffraction data.

(ii) At the Sn edge, the Sn–O shell radius is found to be shorter than the average In–O shell radius ($R = 2.05$ Å, with 5.8 oxygens). This Sn–O configuration looks like an $M1$ site.

As a consequence, cation ordering in $In_4Sn_3O_{12}$ is found when the sixfold-coordinated $M1$ sites are fully occupied by tin, with one-third of the sevenfold-coordinated $M2$ sites occupied by tin atoms and the remaining sites by indium atoms.

Cation ordering in M_7O_{12} occurs when the cation sizes are different enough to change the metal–oxygen bond strength (29). The cation with smaller size and higher charge occupies the $M1$ site, with a shorter M–O distance and
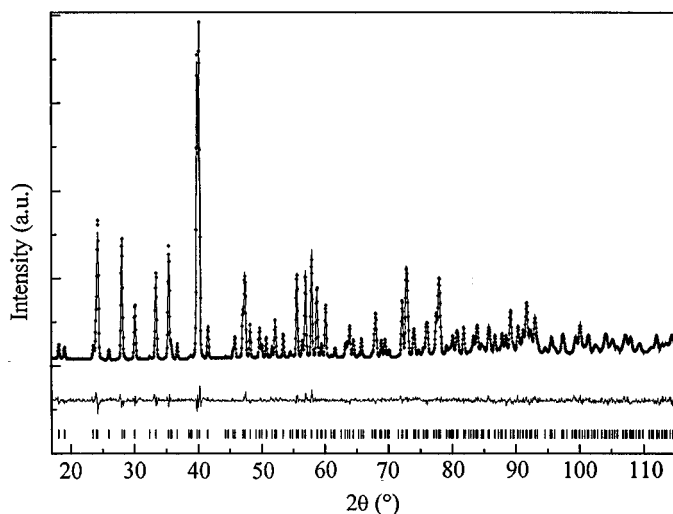
FIG. 7. Observed, calculated, and differential neutron powder diffraction profiles of $In_4Sn_3O_{12}$ (Bragg positions are marked underneath).

○ Oxygen (O_1) ∘ M1
                  ∘ M2
○ Oxygen (O_2) · vacant fluorite-type site

FIG. 8. Hexagonal unit cell for $In_4Sn_3O_{12}$. $M1$–O bonds are marked as black segments.

a lower coordination than the $M2$ site. Complete ordering has been found in UY_6O_{12} and ULu_6O_{12} [$M1$ sites are occupied by U^{6+} ($r = 0.80$ Å) rather than by Y^{3+} ($r = 0.92$ Å) or Lu^{3+} ($r = 0.85$ Å) (26)] and in $Sc_4Ti_3O_{12}$ [$M1$ sites are occupied by Ti^{4+} ($r = 0.68$ Å) rather than Sc^{3+} ($r = 0.81$ Å) 29)]. In contrast, no cationic ordering has been found in $Sc_4Zr_3O_{12}$, which could be due to the similarity in size of the two cations (Zr: 0.79 Å and Sc: 0.81 Å). As shown by EXAFS and neutron diffraction, cation ordering occurs in $In_4Sn_3O_{12}$ where the $M1$ sites are occupied by the smaller cation Sn^{4+} ($r = 0.71$ Å) rather than In^{3+} ($r = 0.81$ Å).

Figure 11 gives the average metal–oxygen distances in various M_7O_{12} compounds where there is a cation order versus the ionic radii of M^{4+} and M^{3+} in $M1$ and $M2$

sites, respectively. The interatomic distances relative to $In_4Sn_3O_{12}$ are also indicated. The mean size of the $M1$ and $M2$ polyhedra is more or less linearly related to the cation radius. The $M1$–V distances are longer than the $M1$–O distances, as a consequence of the $M1$ cation's relaxation from the ideal fluorite position away from the empty anionic

TABLE 4
Interatomic Distances (Å) and Bond Angles (Deg) in $In_4Sn_3O_{12}$

Polyhedron around $M1$			Polyhedron around $M2$		
$M1$–O1	×6	2.057(2)	$M2$–$O1_{(a)}$	×1	2.118(3)
$O1_{(a)}$–$O1_{(b)}$	×6	2.722(3)	$M2$–$O1_{(b)}$	×1	2.145(3)
$O1_{(a)}$–$O1_{(c)}$	×6	3.085(3)	$M2$–$O1_{(c)}$	×1	2.643(3)
$O1_{(a)}$–$M1$–$O1_{(b)}$	×6	82.9(1)	$M2$–$O2_{(a)}$	×1	2.070(3)
$O1_{(a)}$–$M1$–$O1_{(c)}$	×6	97.1(1)	$M2$–$O2_{(b)}$	×1	2.146(3)
			$M2$–$O2_{(c)}$	×1	2.178(3)
			$M2$–$O2_{(d)}$	×1	2.313(3)
Metal–metal distances			Average		2.230
$M1$–$M2$	×6	3.818(2)			
$M1$–$M2$	×6	3.497(2)			
$M2$–$M2$	×1	3.381(3)	Polyhedron around V		
$M2$–$M2$	×2	3.418(3)	V–O1	×3	2.140(2)
$M2$–$M2$	×2	3.474(3)	V–O2	×3	2.292(3)
$M2$–$M2$	×2	3.506(3)	V–$M1$	×1	2.212(2)
$M2$–$M2$	×3	3.864(3)	V–$M2$	×3	2.401(3)

Inversion triad axis
$[111]_F$ or $[0001]_{hex}$

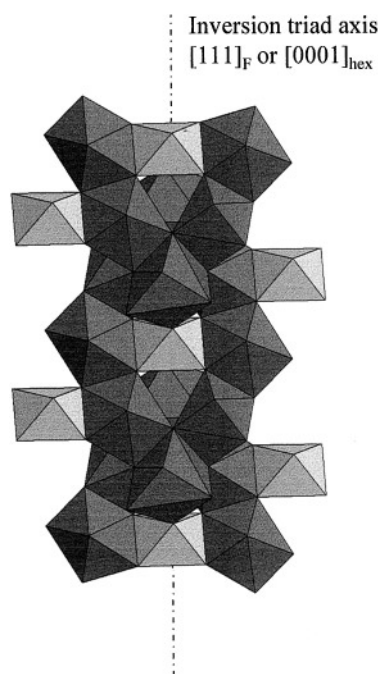FIG. 9. The stacking sequence for sixfold-coordinated $M1$ sites (light gray) and sevenfold-coordinated $M2$ sites (dark gray) along the $[111]_{fluorite}$ axis.
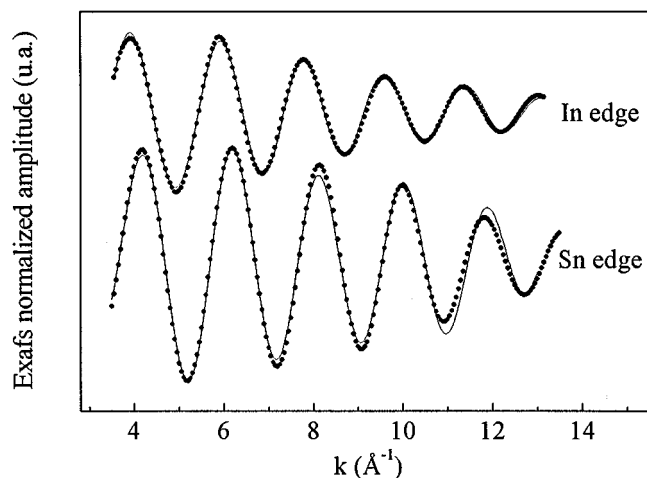
FIG. 10. EXAFS contribution for the first M–O shell in $In_4Sn_3O_{12}$ (In and Sn K-edges): full line, experimental data; dotted line, calculated data.

position (which possesses a formal charge of $+2$). For $In_4Sn_3O_{12}$, the $M1$–V distance is 2.21 Å whereas the metal–oxygen distance in the corresponding fluorite structure is 2.19 Å. The $M1$–V distances versus cation radii exhibit a similar trend as $M1$–O or $M2$–O.

Discussion

The EXAFS and Mössbauer data are compatible with a relaxation of the Sn–O shell in ITO toward a configuration similar to that of the $M1$ site (six oxygen atoms at 2.06 Å) in $In_4Sn_3O_{12}$. A neutron diffraction study shows that the oxygen–cation ratio is higher in ITO than in In_2O_3, which is consistent with the presence of sevenfold-coordinated cationic sites, as found in $In_4Sn_3O_{12}$. The coordina-

FIG. 11. Average metal–oxygen distances in $M1$ and $M2$ sites of the M_7O_{12} compounds versus cation ionic radii (27–30).

tion of oxygens changes from four in In_2O_3 to three around $M1$ sites in $In_4Sn_3O_{12}$. Thus, the tin cation in $M1$-like sites cannot provide one free electron, as observed when it occupies b or d sites. The decrease in the carrier density in ITO could be due to the formation of electrically neutral $In_4Sn_3O_{12}$-like configurations within the indium oxide network. The tin neutralization effect increases when the tin content and oxygen partial pressure increase, because the low-conduction phase exhibits higher tin/indium and oxygen/cation ratios than ITO. The formation of $In_4Sn_3O_{12}$ in ITO can be explained as follows: The existence of a high-temperature and high-pressure C-type rare-earth oxide–corundum transition has been earlier reported for In_2O_3 and Tl_2O_3 (30, 31). The corundum-like In_2O_3 phase is 2.5% denser than the cubic one, where the first In–O shell is described by three oxygens at 2.07 Å and three others at 2.27 Å. The transition was said to be favored by addition of foreign atoms with ionic radii smaller than that of indium and with a cation/oxygen ionic radii ratio equal to 0.6 (32) Indeed, doping by tin ($r_{Sn}^{4+} = 0.71$ Å, $r_{In}^{3+} = 0.81$ Å, $r_{Sn}^{4+}/r_O^{2-} = 0.6$) leads to a rhombohedral modification in ITO powders (33) and in ITO thin films (5) under ambient pressure. These results do not disagree with the presence of a rhombohedral $In_4Sn_3O_{12}$ phase in highly doped ITO bulk materials, since the structure of $In_4Sn_3O_{12}$ exhibits similarities with corundum-like In_2O_3. In particular, $In_4Sn_3O_{12}$ has a higher density and shorter cation–oxygen bonds than cubic In_2O_3 and, therefore, can be compared with high-pressure distorted C-type rare-earth oxides.

In the same way, structural similarities can be found between the cationic polyhedra in $In_4Sn_3O_{12}$ and the tin oxide neutral clusters, as described by Frank (4). The common point arises from the sevenfold coordination of some tin sites, even if we assume that most neutral tin atoms in ITO are located in $M1$ six-fold coordinated sites. The main difference between the two approaches lies in the extension of such neutral-tin configurations. The thin-film deposition methods lead to metastable highly doped phases where the In_2O_3 network is strongly distorted. In contrast, high-temperature syntheses of ITO powders reduce the ability of the In_2O_3 network to accept the deformations induced by tin and help the development of long-range order, which corresponds to a symmetry break, as in the cubic–corundum In_2O_3 transition.

Parent *et al.* (5) found a shortening of the Sn–O distance in ITO films and concluded that the tin environment in films is similar to that in SnO_2, with four oxygens at 2.03 Å and two others at 2.07 Å. This assertion is supported by the formation of crystallized SnO_2 in highly doped ITO films annealed for sufficient time [2 weeks at 950°C (8)]. This result is compatible with our EXAFS data, where tin sites in SnO_2 and in ITO ceramics show similar features. However, no SnO_2 crystallized phase was detected in the ITO ceramics. Yamada *et al.* (22) suggested an electrically inactive tin
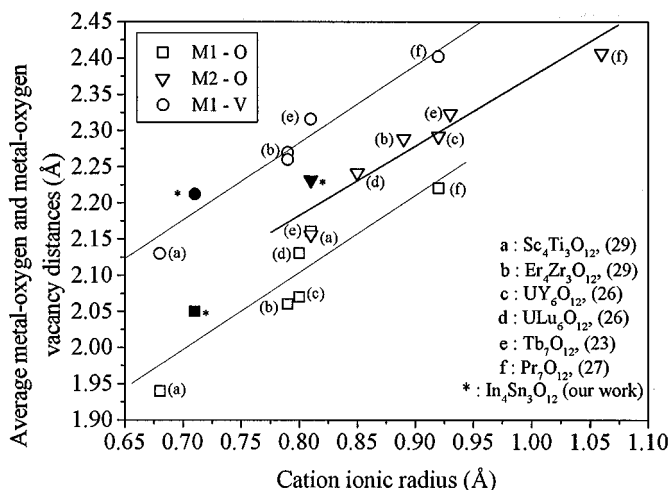
in ITO, by deconvoluting the Mössbauer spectra into two doublets (*b* and *d* sites) plus a singlet (SnO_8 fluorite-like cubic clusters). However, the existence of neutral eightfold-coordinated tin sites may be questioned, because the tin-rich area of the In_2O_3–SnO_2 phase diagram corresponds to the formation of $In_4Sn_3O_{12}$ where the highest oxygen coordination of tin is seven. Finally, TEM observations on oxidized ITO ceramics (6% Sn) do not show a tin-rich phase along the grain boundaries, as observed by Shigesato in ITO films (7).

CONCLUSIONS

The main conclusions of the present study are as follows:

(i) The solubility of tin in indium oxide is $\approx 6\%$. The insertion of tin increases the lattice parameter of ITO ($a = 10.1247(2)$ Å for 6% Sn ITO instead of $10.1195(2)$ Å for In_2O_3). The $In_4Sn_3O_{12}$ rhombohedral phase precipitates at higher concentrations of tin.

(ii) The electrical conductivity of ITO ceramics is lower than would be expected when considering the doping content. The neutralization of the tin donor effect is more marked at high doping level and high oxygen partial pressure.

(iii) The presence of tin results in major changes in the first oxygen polyhedron. The Sn–O distance becomes shorter and the overall oxygen/cation ratio increases as the tin content and oxygen partial pressure increase.

(iv) The structure of $In_4Sn_3O_{12}$ is determined by neutron powder diffraction. It looks like a fluorite-related, non-stoichiometric M_nO_{2n-2} phase with ordering of anion vacancies. EXAFS and neutron diffraction data show that the sixfold-coordinated sites ($M1$) are occupied by tin cations whereas the sevenfold-coordinated sites ($M2$) are occupied by both tin and indium cations.

(v) Mössbauer and EXAFS data in ITO are compatible with a relaxation of the Sn–O shell toward a configuration similar to what is found in tin-rich $In_4Sn_3O_{12}$. This configuration can occur when there is a high probability of finding tin atoms and interstitial oxygens as neighbors. The tin neutralization in ITO is thought to be related to the presence of $M1$-like sites where tin cations are electrically inactive due to a ternary coordination of surrounding oxygens, similar to SnO_2.

This study shows that even a small quantity of tin results in a change between the structures of In_2O_3 and ITO. Although indium is close to tin in the periodic table, the extra electron carried by tin causes a much higher affinity for oxygen. Even if there is a parallelism between ITO ceramics and films, the state of equilibrium that can be reached in sintered ceramics does not allow the existence of amorphous phases of widely varying compositions, as found in thin films.

REFERENCES

1. J. C. C. Fan and F. J. Bachner, *J. Electrochem. Soc.* **122,** 1719 (1975).
2. W. G. Haines and R. H. Bube, *J. Appl. Phys.* **49**(1), 223 (1978).
3. M. Mizuhashi, *Thin Solid Films* **70,** 91 (1980).
4. G. Frank and H. Köstlin, *Appl. Phys. A*: *Solids Surf.* **27,** 197 (1982).
5. Ph. Parent, H. Dexpert, G. Tourillon, and J.-M. Grimal, *J. Electrochem. Soc.* **139**(1), 276 (1992).
6. A. E. Solov'eva and V. A. Zhadnov, *Izv. Akad. Nauk SSR, Neorg. Mater.* **21**(6), 957 (1960).
7. Y. Shigesato, S. Takaki, and T. Haranou, *Appl. Surf. Sci.* **48–49,** 269 (1991).
8. G. Frank, H. Köstlin, and A. Rabenau, *Phys. Status Solidi A* **52,** 231 (1979).
9. M. B. Varfolomeev, A. S. Mironova, F. K. Chibirova, and V. E. Plyushchev, *Inorg. Mater.* **11,** 1926 (1975).
10. H. Enoki, J. Echigoya, and H. Suto, *J. Mater. Sci.* **13,** 192 (1975).
11. J. L. Bates, C. W. Griffin, D. D. Marchant, and J. E. Garnier, *Am. Ceram. Soc. Bull.* **65**(4), 673 (1986).
12. H. Enoki and J. Echigoya, *Phys. Status Solidi A* **132,** K1 (1992).
13. N. Nadaud, M. Nanot, and P. Boch, *J. Am. Ceram. Soc.* **77**(3), 843 (1994).
14. J. Rodriguez-Carvajal, "Powder Diffraction Satellite Meeting of the XVth Congress of the IUA, Toulouse, France." Abst., p.127, 1990.
15. D. Bonnin, P. Kaiser, and J. Desbarres, Ecole CNRS, Garchy, "Structures fines d'absorption des RX. Des données expérimentales à leur analyse." ESPCI, Paris, 1992.
16. Y. Kanai, *Jpn. J. Appl. Phys.* **23**(1), 127 (1984).
17. Y. Shigesato and D. C. Paine, *Appl. Phys. Lett.* **62**(11), 1268 (1993).
18. M. Marezio, *Acta Crystallogr.* **20,** 723 (1966).
19. N. Nadaud and J. Jové, Conference Proceedings ICAME'95, **50,** 565 (1996).
20. K. Nomura, Y. Ujihira, S. Tanaka, and K. Matsumoto, *Hyperfine Interact.* **42,** 1207 (1988).
21. R. C. Mercader, F. H. Sanchez, L. A. Mendoza-Zelis, L. Terminiello, A. G. Bibiloni, C. P. Massolo, J. Desimoni, and A. R. Lopez-Garcia, *Hyperfine Interact.* **23,** 211 (1985).
22. N. Yamada, Y. Shigesato, I. Yasui, H. Li, Y. Ujihira, and K. Nomura, Conference Proceedings ISIAME'96, in press.
23. J. Zhang, R. B. Von Dreele, and L. Eyring, *J. Solid State Chem.* **104,** 21 (1993).
24. M. R. Thornber and D. J. M. Bevan, *J. Solid State Chem.* **1,** 536 (1970).
25. M. R. Thornber, D. J. M. Bevan, and J. Graham, *Acta Crystallogr. B* **24,** 1183 (1968).
26. S. F. Bartram, *Inorg. Chem.* **5,** 749 (1966).
27. R. B. Von Dreele, L. Eyring, A. L. Bowman, and J. L. Yarnell, *Acta Crystallogr. B* **31,** 971 (1975).
28. B. F. Hoskins and R. L. Martin, *J. Chem. Soc., Dalton Trans.* **8,** 676 (1976).
29. H. J. Rossell, *J. Solid State Chem.* **19,** 103 (1970).
30. A. N. Christensen, N. C. Broch, O. Heidenstam, and A. Nilsson, *Acta Chem. Scand.* **21,** 1046 (1967).
31. C. T. Prewit, R. D. Shannon, D. B. Rogers, and A. W. Sleight, *Inorg. Chem.* **8**(9), 1985 (1969).
32. R. W. G. Wyckoff, *in* "Crystal Structures," Vol. 2, p. 6. Interscience Publishers, New York, 1964.
33. G. Frank, R. Olazcuaga, and A. Rabenau, *Inorg. Chem.* **16**(5), 1251 (1977).